JACS
JOURNAL OF THE AMERICAN CHEMICAL SOCIETY

Article

pubs.acs.org/JACS

Reverse Water–Gas Shift on Interfacial Sites Formed by Deposition of Oxidized Molybdenum Moieties onto Gold Nanoparticles

Ronald Carrasquillo-Flores,[†] Insoo Ro,[†] Mrunmayi D. Kumbhalkar,[†] Samuel Burt,[†,‡] Carlos A. Carrero,[‡] Ana C. Alba-Rubio,[†] Jeffrey T. Miller,[§] Ive Hermans,[†,‡] George W. Huber,[†] and James A. Dumesic*[,†]

[†]Department of Chemical and Biological Engineering, University of Wisconsin-Madison, 1415 Engineering Drive, Madison, Wisconsin 53706, United States

[‡]Department of Chemistry, University of Wisconsin-Madison, 1101 University Avenue, Madison, Wisconsin 53706, United States

[§]Chemical Science and Engineering, Argonne National Laboratory, Argonne, Illinois 60439, United States

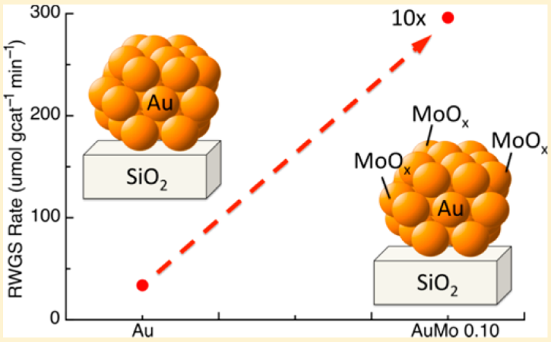

ABSTRACT: We show that MoO$_x$-promoted Au/SiO$_2$ catalysts are active for reverse water–gas shift (RWGS) at 573 K. Results from reactivity measurements, CO FTIR studies, Raman spectroscopy, and X-ray absorption spectroscopy (XAS) indicate that the deposition of Mo onto Au nanoparticles occurs preferentially on under-coordinated Au sites, forming Au/MoO$_x$ interfacial sites active for reverse water–gas shift (RWGS). Au and AuMo sites are quantified from FTIR spectra of adsorbed CO collected at subambient temperatures (e.g., 150–270 K). Bands at 2111 and 2122 cm^{-1} are attributed to CO adsorbed on under-coordinated Au^0 and Au$^{\delta+}$ species, respectively. Clausius–Clapeyron analysis of FTIR data yields a heat of CO adsorption (ΔH_{ads}) of −31 kJ mol^{-1} for Au^0 and −64 kJ mol^{-1} for Au$^{\delta+}$ at 33% surface coverage. Correlations of RWGS reactivity with changes in FTIR spectra for samples containing different amounts of Mo indicate that interfacial sites are an order of magnitude more active than Au sites for RWGS. Raman spectra of Mo/SiO$_2$ show a feature at 975 cm^{-1}, attributed to a dioxo $(O{=})_2Mo({-}O{-}Si)_2$ species not observed in spectra of AuMo/SiO$_2$ catalysts, indicating preferential deposition of Mo on Au. XAS results indicate that Mo is in a +6 oxidation state, and therefore Au and Mo exist as a metal–metal oxide combination. Catalyst calcination increases the quantity of under-coordinated Au sites, increasing RWGS activity. This strategy for catalyst synthesis and characterization enables quantification of Au active sites and interfacial sites, and this approach may be extended to describe reactivity changes observed in other reactions on supported gold catalysts.

INTRODUCTION

Decades after the seminal work of Haruta and co-workers on gold-catalyzed oxidation of CO,[1,2] highly dispersed supported gold nanoparticles continue to receive considerable attention for an increasing number of reactions, including hydrogen dissociation,[3,4] formic acid decomposition,[5,6] water–gas shift (WGS),[7−10] and the selective and total oxidation of hydrocarbons.[11,12] To date, the major factors contributing to catalytic activity are thought to be under-coordinated Au atoms,[5,13] the geometry of the Au clusters,[14,15] the oxidation state of Au atoms,[16−18] and the interface between Au and the metal oxide support.[3,19−21] In spite of considerable research in this area, there is still uncertainty in the identification and quantification of the catalytically active sites for gold catalysts.

Activation of reactants at the Au-metal oxide interface is widely proposed to be a key step for reactions such as H_2 dissociation,[4,22] CO oxidation,[19,23−27] WGS, and reverse water–gas shift (RWGS).[28−37] Rodriguez et al. studied WGS over Au/TiO$_2$(110), and on the basis of experiments and theoretical calculations they concluded that the metal–support interface is critical for the activation of water and the formation of a carboxyl intermediate which further decomposes into CO$_2$ and H$_2$.[29] Ribeiro and co-workers elucidated the effect of the interface on water activation and determined that the WGS reaction rate scales linearly with the number of under-coordinated Au atoms, estimated from physical models of Au clusters and particle size measurements.[8,10] Under-coordinated perimeter and corner sites were found to dominate the reactivity, with corner sites being more active than perimeter sites.[8] These studies illustrate the importance of determining the number of sites at the Au-metal oxide interface.

The RWGS reaction has recently received attention due to the possibility of using CO$_2$ as a source of CO for producing liquid fuels and chemicals through existing technologies, such as methanol synthesis and Fischer–Tropsch synthesis.[38−42] Consequently, it is important to develop fundamental understanding of supported Au catalysts used in the reduction of CO$_2$. Standard chemisorption techniques are not typically used for supported Au catalysts to measure the number of surface metal sites because of weak adsorption on gold surfaces. A promising approach in this respect, however, is to probe surface

Received: June 8, 2015
Published: July 30, 2015

DOI: 10.1021/jacs.5b05945
J. Am. Chem. Soc. 2015, 137, 10317−10325

sites on Au using CO adsorption,[4,9,10,43−52] especially at subambient temperatures. Accordingly, in the present work we have explored this approach to identify and quantitatively assess the metallic and interfacial active sites involved in the RWGS reaction over supported Au catalysts. In these studies, we have used Au/SiO_2 catalysts to study the activity of under-coordinated Au sites, and we then have modified these catalysts with molybdenum oxide moieties using a recently described synthesis approach based on controlled surface reactions (CSR).[53] Using this methodology, Hakim et al. demonstrated it is possible to uniformly deposit Mo moieties on supported Pt nanoparticles with negligible deposition on the support.

Previous research has demonstrated that under-coordinated sites are involved in the chemistry for the majority of Au-catalyzed reactions, whereas the more close-packed facets are generally inert.[3−12] Therefore, we hypothesize that the deposition of Mo will selectively occur on these under-coordinated sites during CSR to prepare AuMo catalysts. To study this hypothesis, we have utilized a variety of characterization tools to probe the effect of Mo on the reactivity of the catalyst, the state of Au and Mo, and the number of active sites under different conditions. Our results provide insight into the nature of the active sites on Au catalysts for RWGS, and in a more general sense, this work demonstrates the efficacy of CSR for AuMo catalysts to quantify and probe the activity of Au and interfacial sites.

■ EXPERIMENTAL METHODS

Catalyst Preparation. A 4 wt % Au/SiO_2 catalyst was prepared by deposition-precipitation. 2.0 g of dry silica (Cab-o-Sil EH-5) was dispersed in 400 mL of a 2 mM chloroauric acid (Sigma-Aldrich) solution at room temperature. The pH of the mixture was adjusted to 9 by dropwise addition of 2.5 M ammonium hydroxide (Sigma-Aldrich). The mixture was aged for 6 h under stirring at room temperature, and the solid material was then filtered and washed with deionized water to remove chloride ions. The sample was dried overnight at 373 K in air. The dried catalyst was reduced in a flow-through cell at a temperature of 623 K (with a heating rate of 2 K min^{-1}) under hydrogen flow (30 cm^3 (STP) min^{-1}) for 4 h. The reduced sample was then transferred to an inert atmosphere glovebox. AuMo/SiO_2 catalysts were prepared by a modified CSR method.[53] A solution of cycloheptatriene molybdenum tricarbonyl (Strem Chemicals) in *n*-pentane (1 mg precursor/g solvent) was added to the 4 wt % Au/SiO_2 catalyst inside a glovebox. The mixture was stirred for 2 h inside the glovebox and transferred to a vacuum oven, where the sample was dried overnight at 318 K. The dried sample was stored inside the glovebox until use. Hereafter, AuMo/SiO_2 samples will be referred to as AuMo X, where X = the Mo/Au atomic ratio. Mo/SiO_2 samples were prepared by depositing the organometallic Mo precursor following the same method as for AuMo/SiO_2.

Reactivity Measurements. RWGS reaction studies were conducted in a fixed-bed down-flow reactor containing 10−15 mg of catalyst packed between quartz wool and silica chips in a 1/4 in. outer diameter stainless steel tube. Control experiments without catalyst determined there was no reactivity from the packing materials and the reactor. The total pressure in the reactor was maintained at 8.1 bar using a back-pressure regulator. Catalysts were heated (2 K min^{-1}) in RWGS flowing gas mixture (H_2:CO_2 2:1 15 cm^3 (STP) min^{-1}) to the reaction temperature at 573 K. After the reactivity measurements were performed, the reactor was cooled to room temperature and then calcined in flowing air at 573 K for 4 h (2 K min^{-1}) and again cooled to room temperature. RWGS reactivity measurements were then carried out at the same conditions as above. The temperature was measured using a K-type thermocouple attached to the outside of the reactor. The temperature of the reactor was adjusted by using a furnace connected to a variable autotransformer, which was controlled with a temperature controller. The reaction temperature was maintained at 573 K, and conversions were maintained below 5% to achieve differential reactor operation. The flow rates for the reactant gases CO_2 and H_2 were fixed using calibrated mass-flow meters (Cole-Parmer FF-32907-59). Research grade CO_2 and ultrahigh purity H_2 (Airgas) were used. The composition of the product gases was analyzed by an online gas chromatograph with a barrier discharge ionization detector (GC-BID) system equipped with an autosampling 6-port valve (Shimadzu). The BID uses helium plasma to detect permanent gases such as CO_2, CO, H_2 with high sensitivity. The GC-BID system was calibrated using Scott specialty gases (P/N 34507 and 34512).

Fourier Transform Infrared Spectroscopy. Catalyst samples were pressed into self-supporting pellets using a 1.2 cm die. Au/SiO_2 and AuMo/SiO_2 pellets were fixed in the sample holder of a transmission cell described elsewhere.[54] The cell was sealed, and the sample was activated in a flowing RWGS gas mixture (H_2:CO_2 2:1) for 4 h at 573 K (2 K min^{-1}). After activation the sample was cooled under RWGS flow to room temperature and then evacuated to 10^{-5} Torr, and a background scan was recorded. Fourier transform infrared (FTIR) (Nicolet 6700) spectra of adsorbed CO were obtained in transmission mode in the presence of 1% CO in He (Airgas). The spectra were collected at temperatures ranging from 148 to 383 K, and the cell was allowed to equilibrate for 5 min at each individual temperature. After the FTIR measurements were performed, the cell was evacuated, and the same pellet was exposed to flowing air. The sample was calcined in air for 4 h at 573 K (2 K min^{-1}) and cooled to room temperature. The sample was reactivated in RWGS flow and analyzed as described above. The temperature was measured by a type-K thermocouple, and heating was controlled by a PID controller (Love Controls Series 16A) connected to a variable autotransformer. The sample holder is designed for collecting spectra at subambient temperatures using flowing liquid nitrogen, as described previously.[54] All data were collected by averaging 256 scans with a resolution of 4 cm^{-1}. Spectral deconvolutions were performed using Origin 9.1 to determine the areal contribution from each peak. The final spectrum of CO adsorbed on each catalyst could be represented by two superimposed Gaussian curves.

Raman Spectroscopy. Raman spectroscopy experiments were carried out using a high-performance Renishaw InVia Raman Spectrometer with a 325 nm (excitation) laser. The laser is a Kimmon IK3201R-F laser with an output of 20 mW and an approximate power of 4 mW at the sample. All measurements used a 2400, l mm^{-1} grating with an efficiency of approximately 30% at 325 nm. *In situ* Raman studies used an OFR near-UV objective with 15× magnification and a working distance of 8.5 mm. Scattered light was filtered into a UV enhanced (lumogen coated) deep depleted array detector (Renishaw). The laser line was calibrated with a Ne calibration lamp. In addition to calibrating the laser, the Raman spectrograph was calibrated to a diamond standard at 1332 cm^{-1}. Raman measurements were taken over a range of 100−1200 cm^{-1} and a dispersion of 1.36565 cm^{-1} $pixel^{-1}$. *In situ* measurements were taken using a fully open aperture and an exposure time of 360 s, with four accumulations. Approximately 10 mg of sample was used for each *in situ* experiment. Experiments were performed in a high-temperature cell (Linkam CCR1000) designed for temperatures up to 1273 K using a quartz window with water-cooled O-rings. The temperature was controlled by a Linkam T95-HT system. Gas flows during *in situ* experiments were controlled by mass flow controllers (Bronkhorst EL-Flow) with maximum flow rates of 50, 100, and 40 cm^3 (STP) min^{-1} for hydrogen, helium, and oxygen/carbon dioxide, respectively. The mass flow controllers were connected to a digital readout system (Bronkhorst series E-7000) capable of mixing gases with variable flow rates. Catalysts were first activated for 2 h at 573 K (10 K min^{-1}), under RWGS flow (H_2:CO_2 2:1 15 cm^3 (STP) min^{-1}). The cell was then flushed with He for 10 min, and the sample was oxidized at 573 K under a flow of 16 cm^3 min^{-1} He (Airgas, UHP) and 4 cm^3 (STP) min^{-1} O_2 (Airgas, Research grade). The sample was oxidized for 2 h prior to obtaining a Raman spectrum. Samples were kept at 573 K for spectra acquisition.

Scanning Transmission Electron Microscopy. Particle size distributions were determined using ImageJ software to analyze

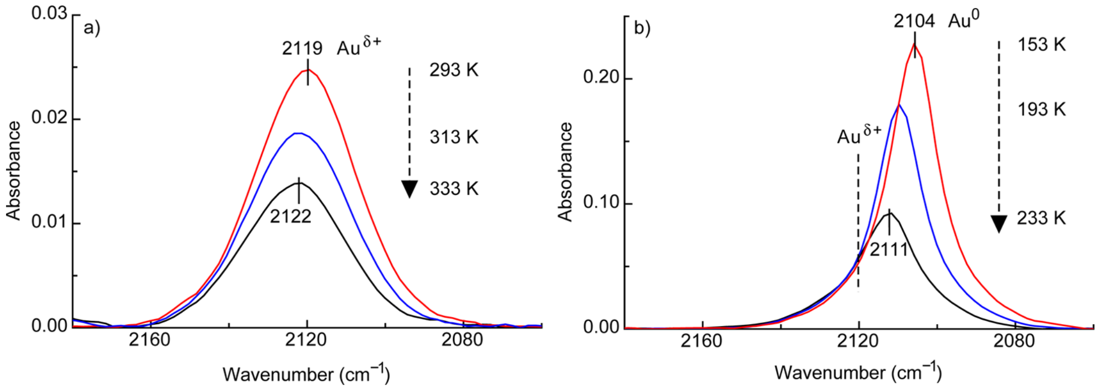

Figure 1. Representative IR spectra at 3×10^{-3} Torr of CO on Au/SiO_2 activated in flowing H_2 at 573 K, showing the (a) Au$^{\delta+}$ band at temperatures higher than 293 K and the (b) Au^0 and Au$^{\delta+}$ bands observed at cryogenic temperatures.

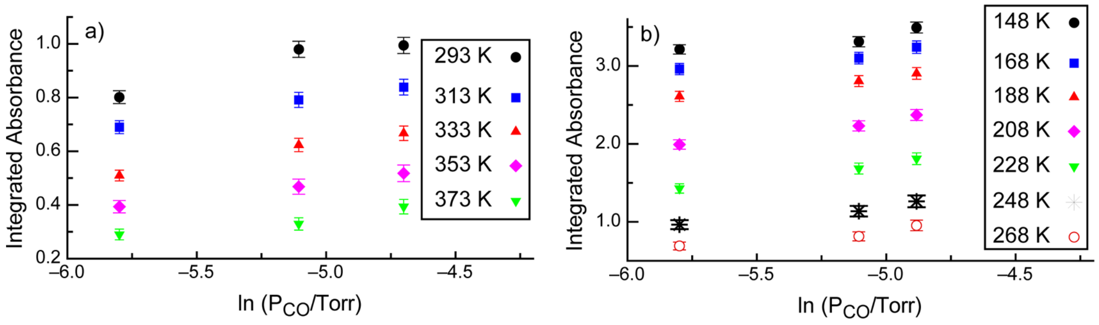

Figure 2. Representative CO adsorption isotherms on Au/SiO_2 activated in flowing H_2 at 573 K for the (a) Au$^{\delta+}$ band and (b) Au^0 band. The integrated absorbance of the Au^0 band was obtained by spectral deconvolution of the original spectrum.

micrographs obtained by scanning transmission electron microscopy (STEM), with at least 1000 nanoparticles considered for each analysis. Images were recorded with an FEI Titan scanning transmission electron microscope with a C_s probe aberration corrector operated at 200 kV with spatial resolution <0.1 nm. The high-angle annular dark-field (HAADF) mode was used, with a HAADF detector angle ranging from 54 to 270 mrad, probe convergence angle of 24.5 mrad, and probe current of ∼25 pA. Energy-dispersive X-ray spectroscopy (EDS) results were obtained with a convergence angle of 24.5 mrad and beam current of 640 pA, with a spatial resolution of 0.5 nm. To prepare samples for STEM, the catalysts were previously activated in a Schlenk tube under RWGS flow at 573 K, cooled to room temperature, sealed, and then opened in a glovebox under N_2 atmosphere to avoid contact with air. The samples were then suspended in ethanol and deposited on carbon-coated copper grids in a N_2 atmosphere. This procedure was previously reported to be an effective method to avoid leaching of oxidized oxophilic components into solution during the ethanol suspension process.[53] STEM samples were plasma cleaned for 15 min before loading into the microscope.

X-ray Absorption Spectroscopy. Au L-edge (11.919 keV) and Mo K-edge (20.000 keV) X-ray absorption spectroscopy (XAS) measurements were performed on the beamlines of the Materials Research Collaborative Access Team (MRCAT, 10-BM and 12-BM) at the Advanced Photon Source (APS) at Argonne National Laboratory. Ionization chambers were optimized to provide maximum current with a linear response (∼10^{10} photons detected s^{-1}). The X-ray beam was 0.25 mm^2, and data were collected in both transmission and fluorescence modes. A third detector in series was used to collect simultaneously a foil reference spectrum with each measurement for energy calibration. All catalysts were pretreated in a continuous-flow reactor, consisting of a quartz tube (1 in. OD, 10 in. length) sealed with Kapton windows by two Ultra-Torr fittings. A ball valve was welded to each Ultra-Torr fitting to enable gas flow through the reactor. An internal type-K thermocouple was fixed against the catalyst sample holder to monitor temperature. Catalyst samples were pressed into a cylindrical sample holder consisting of six wells, each forming a self-supporting pellet. The mass of catalyst was selected to give an absorbance of approximately 1.0. The catalysts were reduced in flowing 3.5% H_2 in He (50 cm^3 (STP) min^{-1}) at 573 K, purged with flowing He for 10 min and then cooled to room temperature. Calcination treatments were performed by flowing air at 573 K, cooling to room temperature and performing the reduction procedure detailed above. XAS spectra were collected for the reduced samples before and after calcination. Traces of oxygen and moisture in the H_2 and He were removed by means of a purifier (Matheson PUR-Gas Triple Purifier Cartridge).

■ RESULTS AND DISCUSSION

Infrared Spectroscopy. To gain insight into the nature of the surface sites present on the various catalysts, FTIR spectra were collected of CO adsorbed on Au and AuMo catalysts over a wide range of temperatures. The spectra in Figure 1 show two features for CO adsorption on two distinct surface sites of Au/SiO_2 activated under H_2 flow at 573 K. These features have been previously observed and have been assigned to the adsorption of CO on under-coordinated Au^0 (2111 cm^{-1}) and CO on under-coordinated Au$^{\delta+}$ (2122 cm^{-1}).[44,45,49,55−57] The spectra at low temperature, Figure 1b, reveal that the majority of the sites are Au^0 when Au is activated under H_2 flow. Spectral deconvolution of the bands collected at 173 K reveals that 74 ± 5% of the total sites are Au^0, assuming that the extinction coefficients of the two bands are equal. We selected 173 K as the temperature for quantification for two reasons: (1) This is the lowest temperature at which CO bands on SiO_2 are not observed; and (2) we have employed this low temperature to achieve a high coverage of CO on the surface sites associated with Au. CO pressures between 3×10^{-3} and 9×10^{-3} Torr were studied, from which we obtained adsorption isotherms

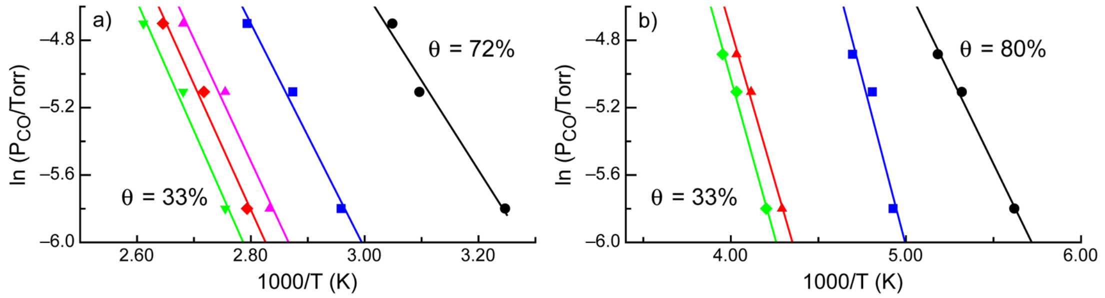

Figure 3. Isosteric plots for CO on Au/SiO_2 activated in flowing H_2 at 573 K for the (a) $Au^{\delta+}$ band and (b) Au^0 band. The surface coverage changes from left to right in (a) as 33%, 36%, 40%, 49%, and 72% and in (b) as 33%, 36%, 63%, and 80%. Constant coverage data points were identified from the full set of data represented by Figure 2. The coverage was calculated by normalizing the absorbance based on the maximum absorbance of the sample for each site obtained through spectral deconvolution. All data were collected on a single catalyst pellet.

(Figure 2). From these data it is possible to identify combinations of temperature and pressure that display the same absorbance (i.e., equal surface coverage), allowing the use of isosteres to perform a Clausius−Clapeyron analysis, Figure 3. We have assumed that the CO IR intensity is linear with coverage. This assumption appears to be valid by the observation that the isosteres are linear over the range of temperatures and pressures where the CO frequency is constant.[58] Moreover, the selected data points used to generate a specific isostere are all at constant absorbance (intensity) and, therefore, at constant surface coverage. Therefore, any effects of coverage on the IR extinction coefficient only shift our reported coverage values but would not affect the calculated heat of CO adsorption. Accordingly we have calculated the isosteric heat of CO adsorption, ΔH_{ads}, from the slope of each isostere. For both Au^0 and $Au^{\delta+}$, the value of ΔH_{ads} increases with decreasing coverage, in agreement with previous work.[44,45] Values of ΔH_{ads} at high coverage, $\theta > 70\%$, and low coverage, $\theta = 33\%$, are reported in Table 1. The value of ΔH_{ads} for Au^0 increases from −18 to −31 kJ mol^{-1} from high to low coverage, respectively. For $Au^{\delta+}$, the value of ΔH_{ads} increases from −44 to −64 kJ mol^{-1}. The value of ΔS_{ads}, derived from the equilibrium constant calculated from the Langmuir isotherm, is also reported at low coverage and was calculated to be −88 J mol^{-1} K^{-1} for Au^0 and −133 J mol^{-1} K^{-1} for Au $^{\delta+}$. The changes in ΔH_{ads} due to coverage effects are consistent with other infrared studies of CO adsorption on Au.[44−46] While both of these sites experience coverage effects, the values of ΔH_{ads} and ΔS_{ads} are higher for $Au^{\delta+}$ compared to Au^0 and indicate a more localized and stronger adsorption for adsorption on the former sites. Further, the coexistence of the Au^0 and $Au^{\delta+}$ sites explains why a two-site Langmuir adsorption model can provide a better representation of CO adsorption data on Au.[8,46] Performing the same analysis of data collected using the AuMo catalysts revealed no significant difference in the values of ΔH_{ads} and ΔS_{ads} between AuMo and Au nanoparticles, indicating that the presence of Mo does not have an effect on the energetics of CO adsorption on Au.

Table 1. Thermodynamic Parameters Determined by Clausius−Clapeyron Treatment of CO Adsorption FTIR Data at a Surface Coverage of 33%

site	ΔH_{ads} (kJ mol^{-1})	ΔS_{ads} (J mol^{-1} K^{-1})
Au^0	−31 ± 3 (−18 ± 1)[a]	−88 ± 3
$Au^{\delta+}$	−64 ± 8 (−44 ± 6)[a]	−133 ± 9

[a] Values in parentheses are values of ΔH_{ads} at high coverage

FTIR spectra of the Au and AuMo catalysts activated under RWGS flow and collected at 3 x10^{-1} Torr of CO are compared in Figure 4. The increase in CO pressure, as compared to Figure 1, was used to increase the uptake of CO onto Au sites and populate as many sites as possible, i.e., to saturate the surface sites on the sample. For as-synthesized Au, Figure 4a, spectral deconvolution of the bands reveals that after RWGS activation only 22 ± 1% of the sites are Au^0, in contrast with 74 ± 5% for H_2 activation. This increase in the intensity of the $Au^{\delta+}$ band occurs at the expense of Au^0 sites that are oxidized from reaction with CO_2 present in the RWGS gas

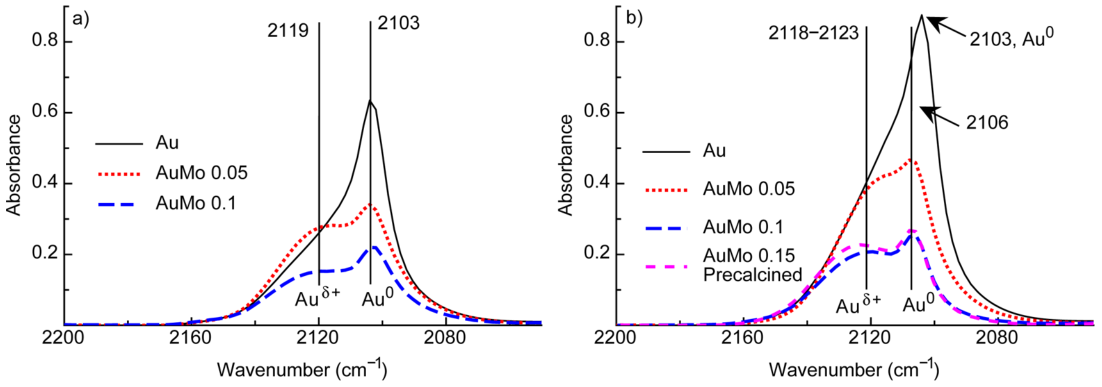

Figure 4. IR spectra for CO adsorbed on (a) as-synthesized and (b) calcined Au/SiO_2 and AuMo/SiO_2 at 173 K and 3 × 10^{-1} Torr of CO. The intensities are normalized by the pellet density. Catalysts were activated in flowing RWGS conditions at 573 K.

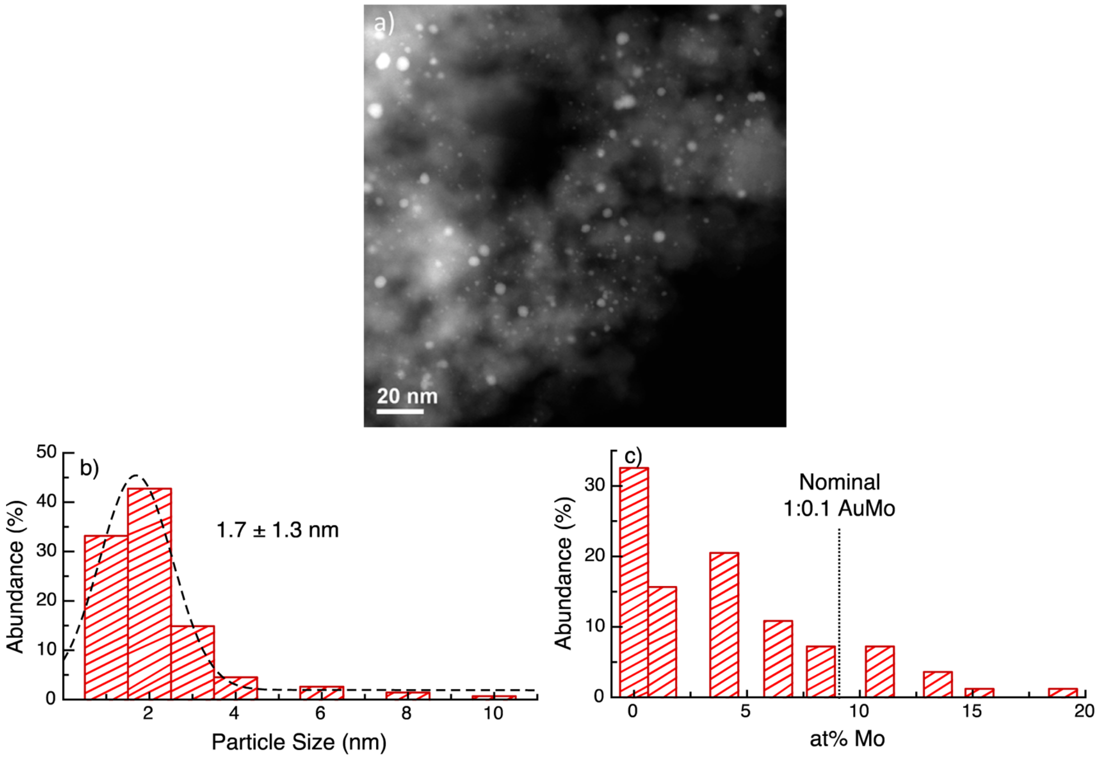

Figure 5. Representative (a) HAADF-STEM image, (b) particle size distribution, and (c) EDS histogram of Mo content for AuMo 0.1 catalyst activated in flowing RWGS conditions at 573 K.

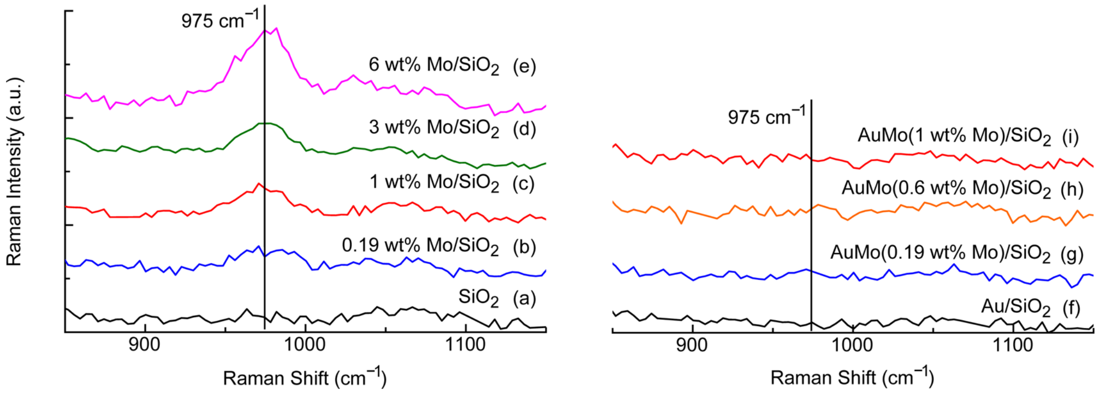

Figure 6. *In situ* Raman spectra (325 nm) of SiO$_2$ and SiO$_2$ supported Mo, Au, and AuMo at 573 K under oxidizing conditions. The vertical line denotes the Raman shift corresponding to the symmetric stretch of a Mo(=O)$_2$ from a dioxo (O=)$_2$Mo(−O−Si)$_2$. (a) SiO$_2$, (b) 0.19 wt % Mo/SiO$_2$, (c) 1 wt % Mo/SiO$_2$, (d) 3 wt % Mo/SiO$_2$, (e) 6 wt % Mo/SiO$_2$, (f) Au/SiO$_2$, (g) AuMo 1:0.1, (h) AuMo 1:0.3, and (i) AuMo 1:0.5.

mixture.[56,57,59,60] This behavior indicates that the original distribution of sites generated during catalyst reduction is altered under RWGS conditions. Additionally, it is important to note that while these results provide insight into the nature of the working catalyst during reaction, the parent Au/SiO$_2$ catalyst was always prereduced before CSR addition of Mo, and therefore the majority of the sites are in a metallic state.

Addition of Mo to as-synthesized Au, Figure 4a, produces a decrease on the CO uptake at 173 K, indicating that the original number of Au sites available for CO binding has been decreased by addition of Mo. Calcination of the samples, Figure 4b, leads to an increase in CO uptake. One possible explanation for the increase in uptake could be a change in the Au particle morphology. Previous work has shown that O$_3$ treatments at cryogenic temperatures can roughen Au(111) surfaces and produce defects.[61] In our case, we have calcined the catalysts in flowing air, and specific to Au catalysts, the activation of O$_2$ has a low activation barrier on step sites as opposed to on extended surfaces.[13] In addition, small Au nanoparticles bind atomic oxygen more strongly than close-packed Au surfaces.[62] From a particle size analysis of STEM micrographs, Figure 5, the average particle size was determined to be 1.7 ± 1.3 nm. Based on existing correlations,[63] the first-shell coordination number (obtained from XAS results) was used to estimate the average particle size as 1.3 nm, which is in agreement with our measurements. Therefore, we believe it is likely that surface roughening occurs during the calcination treatment and that more under-coordinated Au sites are exposed on the roughened nanoparticles, which would account for the observed promotional effect of calcination. To further investigate the effect of the calcination, CSR of Mo onto Au (Mo:Au = 0.15) was performed using calcined Au/SiO$_2$ as the parent material

(Figure 4b), as a method to increase the number of low coordination sites on the Au nanoparticles prior to deposition of Mo. The CO uptake for this catalyst was equal to that of the AuMo catalyst with Mo:Au = 0.1. This result suggests that the maximum amount of Mo that can be added selectively to the under-coordinated Au sites on the Au/SiO_2 catalyst of the present study corresponds to Mo:Au = 0.15. As will be discussed in the Raman section, higher amounts of Mo can be deposited onto Au; however, reactivity measurements for samples with higher Mo loading showed lower reactions rates. In addition, infrared measurements for these catalysts showed no correlation between the Mo content and the intensity of the CO bands. These results could indicate the formation of Mo clusters on Au at higher Mo contents.

Raman Spectroscopy and X-ray Absorption Spectroscopy. Figure 6 shows Raman spectra for all of the AuMo catalysts as well as for different Mo/SiO_2 samples. The feature at 975 cm^{-1}, present for all Mo/SiO_2 samples and increasing with Mo loading, corresponds to the symmetric stretch of $Mo(=O)_2$ from a dioxo $(O=)_2Mo(-O-Si)_2$ surface species commonly observed for samples consisting of MoO_3 dispersed on SiO_2.[64,65] This feature is not present on SiO_2, Au/SiO_2, or the AuMo/SiO_2 catalysts. We also performed EDS analysis of the Mo content for AuMo 0.1, Figure 5c, and the results indicate that in the majority of the particles analyzed (67%), Mo has been deposited on Au nanoparticles. Higher Mo loading samples were prepared, up to AuMo 1:0.5 (1 wt % Mo), to promote the evolution of the band. However, we did not observe the $Mo(=O)_2$ stretch even at these high Mo loadings. The presence of the $Mo(=O)_2$ stretch for the Mo/SiO_2 samples indicates that the sensitivity of the Raman spectrometer is sufficient to detect these species at the loadings employed in the present study. Importantly, the absence of this band for AuMo samples is evidence for the deposition of Mo on Au and not on SiO_2. Taken together with the FTIR results, these observations suggest the formation of AuMo sites via selective Mo deposition on Au.

X-ray absorption near edge spectroscopy (XANES) was used to determine the extent of Mo oxidation in the Mo/SiO_2 and AuMo/SiO_2 samples. Fluorescence data, Figure 7, were collected after the samples were calcined and reduced in H_2. According to fits of the XANES curves, Mo in the analyzed Mo and AuMo samples is in a high oxidation state (e.g., Mo^{6+}). Importantly, this result suggests that Au and Mo exist as a metal–metal oxide combination, and not as a bimetallic alloy, as has been observed for the case of PtMo.[66] Transmission spectra for samples with higher Mo loading, Figure 8, indicate a slightly different behavior for these materials. In particular, when the AuMo samples are only pretreated in hydrogen, the Mo is in a slightly reduced state, existing as a mixture of Mo^{4+} and Mo^{6+}. Calcination of this same sample, however, leads to oxidation of the Mo, and only Mo^{6+} was observed. Altogether, the XANES results indicate that the Au–Mo interactions observed in FTIR and Raman spectroscopy results stem from Au-MoO_x species.

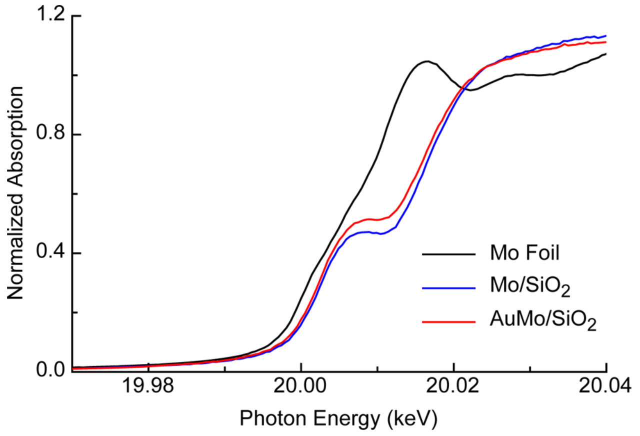

Figure 7. XANES fluorescence data characterizing reduced (573 K) Au/SiO_2 and AuMo/SiO_2 after calcination at 573 K. The Mo loading for all samples was 0.2 wt % (AuMo 0.1).

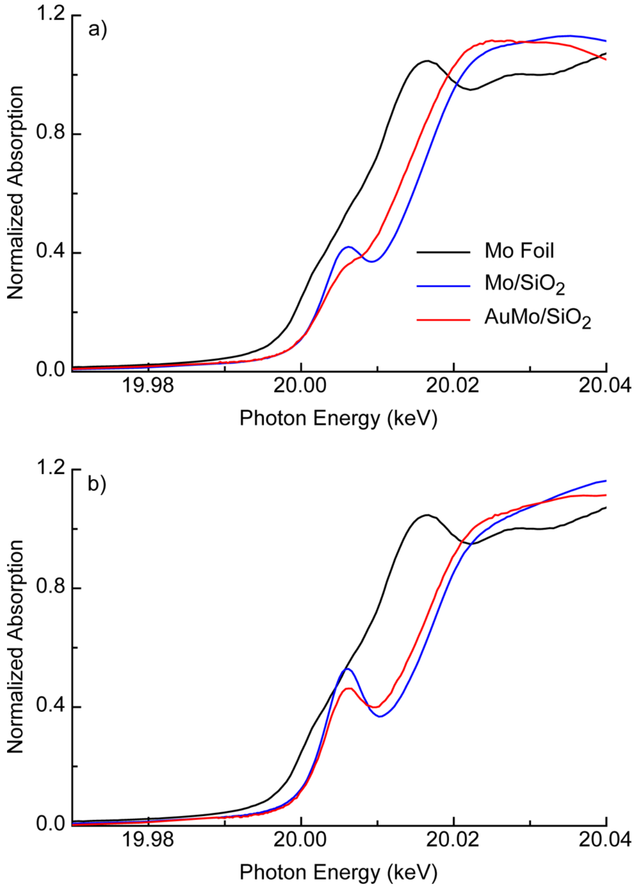

Figure 8. XANES transmission data characterizing reduced SiO_2-supported samples after (a) reduction and (b) calcination at 573 K. The Mo loading for all samples was 1 wt % (AuMo 0.5).

Reactivity Measurements. The catalytic properties of Au/SiO_2 and AuMo/SiO_2 were studied for the RWGS reaction (573 K, 8.1 bar) in a packed bed reactor. Figure 9 shows the reactivity of the Au and AuMo catalysts. Deposition of Mo onto Au/SiO_2 by CSR increases the rate at all Mo levels as compared to Au/SiO_2. Calcination of the catalysts increases the rate measured for all of the catalysts, but the effect of the calcination is more marked at lower Mo levels. This result agrees with the infrared measurements shown in Figure 4, where the CO uptake after calcination shows a higher increase at low Mo loadings. Importantly, while calcined Au shows the highest increase in the rate compared to its as-synthesized counterpart (by a factor of 3), the rate for as-synthesized AuMo 0.1 is an order of magnitude higher than that of as-synthesized Au. This result indicates that a combination of Au and interfacial AuMo

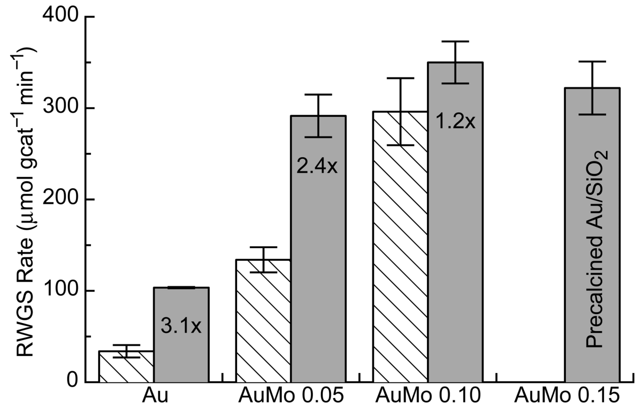

Figure 9. RWGS at 573 K and 8.1 bar of H_2:CO_2 (2:1) for as-synthesized (hashed bars) and calcined (gray bars) Au/SiO_2 and AuMo/SiO_2. Numbers inside the gray bars show the increase in the rate after calcination.

sites formed during CSR is more active than Au sites alone. The reaction rate for AuMo 0.15 is essentially equal to that of the calcined AuMo 0.1, in agreement with the infrared measurements for these two catalysts.

Active Sites. The FTIR, Raman, XANES, and reactivity data for our catalysts provide information about the species present during synthesis conditions and reactions. First, Au sites in the studied catalysts exist in the form of Au^0 and $Au^{\delta+}$ species, and the abundance of each site is related to the conditions under which the catalyst is treated. Second, Au sites can bind Mo during our CSR method of deposition, preventing CO uptake on these sites and forming interfacial AuMo sites. Third, the Mo bound to under-coordinated Au is in a high oxidation state. And finally, a combination of Au sites and interfacial AuMo sites is more active for RWGS than Au sites alone. From this information, two types of active sites for RWGS are present and are designated as Au sites, including Au^0 and $Au^{\delta+}$, and AuMo interfacial sites. We can estimate the number of each type of site using a combination of STEM and FTIR spectroscopy of adsorbed CO. The average particle size obtained from STEM micrographs, Figure 5, is 1.7 ± 1.3 nm and can be used to estimate the number of terrace, perimeter, and corner sites based on physical models of Au clusters described in the literature.[7−9] It has previously been shown that WGS activity using Au/Al_2O_3 catalysts correlated with the number of perimeter and corner sites (i.e., the number of under-coordinated sites);[8] therefore, we will assume that this value corresponds to the number of active Au sites on our catalysts. Based on this approach, the number of Au sites that adsorb CO is estimated to be 59.5 μmol gcat^{-1}. It is important to note that the initial site density is expected to be equal for all as-synthesized catalysts, because the addition of Mo was always carried out using the same Au/SiO_2 parent material.

An alternative approach to estimate the number of under-coordinated Au sites is to assume that the deposition of Mo occurs on these sites with a 1:1 stoichiometry. Based on the change in the integrated CO FTIR area with the addition of increasing amounts of Mo, as shown in Table 2, it is necessary to have approximately 40 μmol gcat^{-1} of under-coordinated Au sites on the as-synthesized Au/SiO_2 sample. Using this value along with the previously used particle size correlations, we estimate a Au particle size of 2 nm, which is within the error of our microscopy measurements. Using this site density we can now calibrate the area of CO absorbance in the FTIR experiments to provide an estimate for the number of under-coordinated Au sites for each catalyst, and these values are reported in Table 2. This analysis demonstrates that by depositing Mo moieties onto Au catalysts and measuring the decrease in CO uptake, we can effectively quantify the number of under-coordinated Au sites without the need to employ particle size correlations.

Using the calculated values for the amount of adsorbed CO, the variation in the number of Au sites measured by FTIR spectra is plotted in Figure 10 versus the number of Mo species deposited onto the Au nanoparticles by our CSR method. These site measurements, in conjunction with the RWGS reaction rates, were then used to estimate the rate contributions from each site. The rate for each catalyst was calculated from the following equation:

$$R_{\text{total}} = S_{\text{Au}}R_{\text{Au}} + S_{\text{AuMo}}R_{\text{AuMo}}$$

Here S_{Au} is the total number of Au sites, including Au^0 and $Au^{\delta+}$, per gram of catalyst as measured by FTIR-CO measurements. Similarly, S_{AuMo} represents the number of AuMo sites (interfacial sites), as determined from the change in the amount of adsorbed CO relative to Au/SiO_2, either as-synthesized or calcined, respectively. R_{Au} and R_{AuMo} are the turnover rates (mole CO produced per mole of Au or AuMo site per minute) relevant to each site. This model involved two parameters, R_{Au} and R_{AuMo}, which were linearly optimized with seven data points for AuMo/SiO_2 catalysts. The results from the model indicate that at the conditions studied, the rate per interfacial site, $R_{\text{AuMo},}$ is approximately 10 times greater than the rate per Au site, R_{Au}, where R_{AuMo} has a value of 10.4 min^{-1} and R_{Au} has a value of 1 min^{-1}. The rate predictions from our model are shown in Figure 11. A parity plot, indicating the goodness of the fit, is shown in Figure 12. Shekhar et al. have previously observed a similar result leading to higher rates of WGS catalyzed by Au/TiO_2 as compared to Au/Al_2O_3.[8] Specifically,

Table 2. Results from FTIR Spectroscopy of CO Adsorbed on SiO_2-Supported Au and AuMo Catalysts

sample	Au:Mo (mole:mole)	pretreatment	Mo deposited (μmol gcat^{-1})	normalized CO FTIR area[b]	adsorbed CO (μmol gcat^{-1})[c]
Au	1:0	RWGS	0	1	41.5 ± 3.1
AuMo	1:0.05	RWGS	10.2	0.83	34.4 ± 4.7
AuMo	1:0.1	RWGS	20.3	0.52	21.6 ± 3.5
Au	1:0	Calcined	0	1.4	58.1 ± 1.8
AuMo	1:0.05	Calcined	10.2	0.99	41.1 ± 1.6
AuMo	1:0.1	Calcined	20.3	0.57	23.7 ± 1.1
AuMo[a]	1:0.15	Calcined	30.5	0.63	26.1 ± 1.3

[a] Au/SiO_2 was calcined at 573 K before Mo deposition was performed [b] Combined integrated area of CO on Au^0 and $Au^{\delta+}$ sites. [c] Calculated from the total number of perimeter and corner sites for a 2 nm average particle size catalyst, 41.5 μmol gcat^{-1}, multiplied by the normalized CO FTIR area

DOI: 10.1021/jacs.5b05945
J. Am. Chem. Soc. 2015, 137, 10317−10325

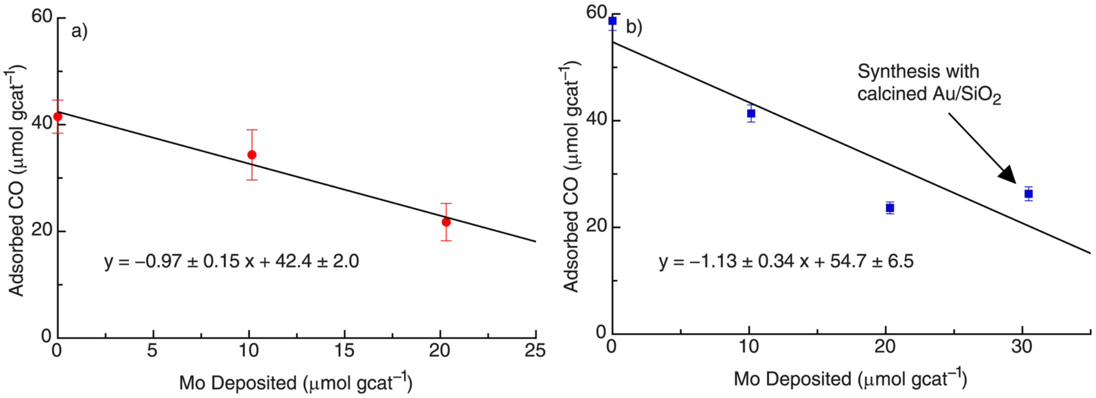

Figure 10. FTIR-CO adsorption data for (a) as-synthesized and (b) calcined samples after Mo deposition.

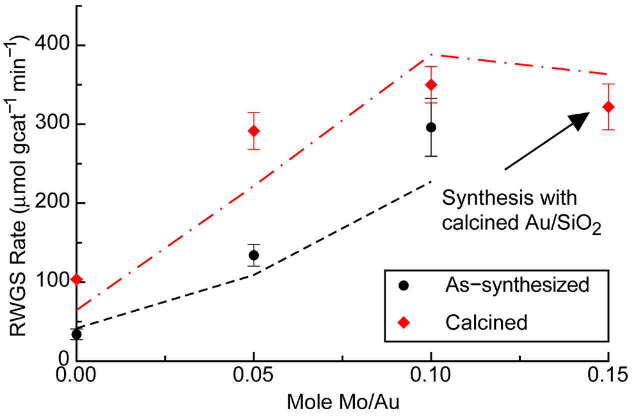

Figure 11. RWGS at 573 K and 8.1 bar of H_2:CO_2 (2:1) for as-synthesized and calcined Au/SiO_2 and AuMo/SiO_2. Dashed lines indicate the rates predicted by our model. The rate per AuMo site is 10 times greater than that of a Au site. The model predictions are R_{Au} = 1 min^{-1} and R_{AuMo} = 10.4 min^{-1}.

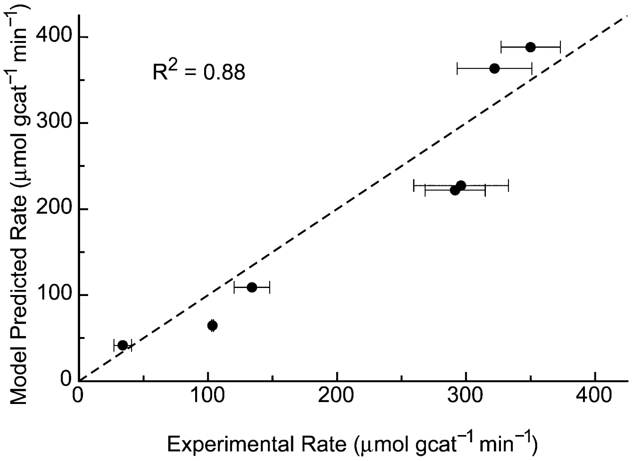

Figure 12. Calculated (model) versus experimental rates for the RWGS reaction.

the promotion effect has been attributed to the capacity of the support/Au-support interface to activate H_2O, producing a higher coverage of hydroxyl species.[8,26] Our Au/SiO_2 catalyst behaves much like Au/Al_2O_3 and exhibits only Au sites for RWGS, whereas our AuMoO_x catalysts possess interfacial sites that complement the Au sites and are responsible for higher catalyst activity, analogous to when TiO_2 is used as the support.

■ CONCLUSIONS

Based on results from RWGS reactivity measurements, CO FTIR spectra, STEM studies, and Raman and XANES analyses, we have demonstrated that the deposition of Mo onto SiO_2-supported Au catalysts occurs on under-coordinated sites of Au nanoparticles to form AuMoO_x interfacial sites that are active for the RWGS reaction. The number of under-coordinated Au sites and the number of AuMo interfacial sites can be determined from FTIR experimental results of CO uptake, and it is shown that the interfacial sites are an order of magnitude more active than Au sites for the RWGS reaction. The presence of Au^0 and $Au^{\delta+}$ sites on Au/SiO_2 and AuMo/SiO_2 was observed, and it was determined that metallic sites are more abundant after reduction, whereas the oxidized sites prevail under RWGS reaction conditions. Calcination of the catalysts roughens the surface of Au nanoparticles and increases the quantity of under-coordinated Au sites, which is responsible for an increase in RWGS activity. Our strategy for catalyst synthesis by controlled deposition reactions, combined with FTIR measurements of adsorbed CO at subambient temperatures, opens the possibility for quantification of both Au active sites and the active interfacial sites. Moreover, this approach can be used to deposit small amounts of the metal-oxide moieties onto the surfaces of Au nanoparticles, demonstrating the potential for this approach to identify and ascribe changes in reactivity and selectivity observed with Au/metal-oxide catalysts for reactions where support effects may be important.

■ AUTHOR INFORMATION

Corresponding Author

*dumesic@engr.wisc.edu

Notes

The authors declare no competing financial interest.

■ ACKNOWLEDGMENTS

This material is based upon work supported by the U.S. Department of Energy, Office of Basic Energy Sciences. We are thankful for the use of the Advanced Photon Source, an Office of Science User Facility operated for the DOE Office of Science by Argonne National Laboratory, supported by the U.S. DOE under contract DE-AC02-06CH11357. We wish to thank Canan Sener for valuable discussions and help in catalyst synthesis

REFERENCES

(1) Haruta, M.; Kobayashi, T.; Sano, H.; Yamada, N. *Chem. Lett.* **1987**, 405.

(2) Haruta, M.; Yamada, N.; Kobayashi, T.; Iijima, S. *J. Catal.* **1989**, *115*, 301.

(3) Fujitani, T.; Nakamura, I.; Akita, T.; Okumura, M.; Haruta, M. *Angew. Chem., Int. Ed.* **2009**, *48*, 9515.

(4) Panayotov, D. A.; Burrows, S. P.; Yates, J. T.; Morris, J. R. *J. Phys. Chem. C* **2011**, *115*, 22400.

(5) Singh, S.; Li, S.; Carrasquillo-Flores, R.; Alba-Rubio, A. C.; Dumesic, J. A.; Mavrikakis, M. *AIChE J.* **2014**, *60*, 1303.

(6) Ojeda, M.; Iglesia, E. *Angew. Chem., Int. Ed.* **2009**, *48*, 4800.

(7) Williams, W. D.; Shekhar, M.; Lee, W. S.; Kispersky, V.; Delgass, W. N.; Ribeiro, F. H.; Kim, S. M.; Stach, E. A.; Miller, J. T.; Allard, L. F. *J. Am. Chem. Soc.* **2010**, *132*, 14018.

(8) Shekhar, M.; Wang, J.; Lee, W. S.; Williams, W. D.; Kim, S. M.; Stach, E. A.; Miller, J. T.; Delgass, W. N.; Ribeiro, F. H. *J. Am. Chem. Soc.* **2012**, *134*, 4700.

(9) Shekhar, M.; Wang, J.; Lee, W.-S.; Cem Akatay, M.; Stach, E. A.; Nicholas Delgass, W.; Ribeiro, F. H. *J. Catal.* **2012**, *293*, 94.

(10) Wang, J.; Kispersky, V. F.; Delgass, W. N.; Ribeiro, F. H. *J. Catal.* **2012**, *289*, 171.

(11) Hayashi, T.; Tanaka, K.; Haruta, M. *J. Catal.* **1998**, *178*, 566.

(12) Stangland, E. E.; Stavens, K. B.; Andres, R. P.; Delgass, W. N. *J. Catal.* **2000**, *191*, 332.

(13) Xu, Y.; Mavrikakis, M. *J. Phys. Chem. B* **2003**, *107*, 9298.

(14) Vilhelmsen, L. B.; Hammer, B. *Phys. Rev. Lett.* **2012**, *108*, 108.

(15) Hakkinen, H.; Abbet, W.; Sanchez, A.; Heiz, U.; Landman, U. *Angew. Chem., Int. Ed.* **2003**, *42*, 1297.

(16) Vilhelmsen, L. B.; Hammer, B. *J. Chem. Phys.* **2013**, *139*, 204701.

(17) Hong, S.; Rahman, T. S. *J. Am. Chem. Soc.* **2013**, *135*, 7629.

(18) Boronat, M.; Illas, F.; Corma, A. *J. Phys. Chem. A* **2009**, *113*, 3750.

(19) Vilhelmsen, L. B.; Hammer, B. *ACS Catal.* **2014**, *4*, 1626.

(20) Bowker, M.; James, D.; Stone, P.; Bennett, R.; Perkins, N.; Millard, L.; Greaves, J.; Dickinson, A. *J. Catal.* **2003**, *217*, 427.

(21) Xiao Yan, L.; Aiqin, W.; Tao, Z.; Chung-Yuan, M. *Nano Today* **2013**, *8*, 403.

(22) Nakamura, I.; Mantoku, H.; Furukawa, T.; Fujitani, T. *J. Phys. Chem. C* **2011**, *115*, 16074.

(23) Biener, M. M.; Biener, J.; Wichmann, A.; Wittstock, A.; Baumann, T. F.; Baumer, M.; Hamza, A. V. *Nano Lett.* **2011**, *11*, 3085.

(24) Kotobuki, M.; Leppelt, R.; Hansgen, D. A.; Widmann, D.; Behm, R. J. *J. Catal.* **2009**, *264*, 67.

(25) Fujitani, T.; Nakamura, I. *Angew. Chem., Int. Ed.* **2011**, *50*, 10144.

(26) Saavedra, J.; Doan, H. A.; Pursell, C. J.; Grabow, L. C.; Chandler, B. D. *Science* **2014**, *345*, 1599.

(27) Li, L.; Wang, A. Q.; Qiao, B. T.; Lin, J.; Huang, Y. Q.; Wang, X. D.; Zhang, T. *J. Catal.* **2013**, *299*, 90.

(28) Mudiyanselage, K.; Senanayake, S. D.; Feria, L.; Kundu, S.; Baber, A. E.; Graciani, J.; Vidal, A. B.; Agnoli, S.; Evans, J.; Chang, R.; Axnanda, S.; Liu, Z.; Sanz, J. F.; Liu, P.; Rodriguez, J. A.; Stacchiola, D. J. *Angew. Chem., Int. Ed.* **2013**, *52*, 5101.

(29) Rodriguez, J. A.; Evans, J.; Graciani, J.; Park, J.-B.; Liu, P.; Hrbek, J.; Fdez Sanz, J. *J. Phys. Chem. C* **2009**, *113*, 7364.

(30) Burch, R. *Phys. Chem. Chem. Phys.* **2006**, *8*, 5483.

(31) Park, J. B.; Graciani, J.; Evans, J.; Stacchiola, D.; Senanayake, S. D.; Barrio, L.; Liu, P.; Sanz, J. F.; Hrbek, J.; Rodriguez, J. A. *J. Am. Chem. Soc.* **2010**, *132*, 356.

(32) Rodriguez, J. A.; Ma, S.; Liu, P.; Hrbek, J.; Evans, J.; Perez, M. *Science* **2007**, *318*, 1757.

(33) Rodriguez, J. A.; Liu, P.; Hrbek, J.; Evans, J.; Perez, M. *Angew. Chem., Int. Ed.* **2007**, *46*, 1329.

(34) Rodriguez, J. A. *Catal. Today* **2011**, *160*, 3.

(35) Wang, X.; Rodriguez, J. A.; Hanson, J. C.; Perez, M.; Evans, J. *J. Chem. Phys.* **2005**, *123*, 221101.

(36) Rodriguez, J. A.; Liu, R.; Hrbek, J.; Perez, M.; Evans, J. *J. Mol. Catal. A: Chem.* **2008**, *281*, 59.

(37) Upadhye, A. A.; Ro, I.; Zeng, X.; Kim, H. J.; Tejedor, I.; Anderson, M. A.; Dumesic, J. A.; Huber, G. W. *Catal. Sci. Technol.* **2015**, *5*, 2590.

(38) Hakim, S. H.; Sener, C.; Alba-Rubio, A. C.; Gostanian, T. M.; O'Neill, B. J.; Ribeiro, F. H.; Miller, J. T.; Dumesic, J. A. *J. Catal.* **2015**, *328*, 75.

(39) Centi, G.; Iaquaniello, G.; Perathoner, S. *ChemSusChem* **2011**, *4*, 1265.

(40) Quadrelli, E. A.; Centi, G.; Duplan, J. L.; Perathoner, S. *ChemSusChem* **2011**, *4*, 1194.

(41) Corma, A.; Garcia, H. *J. Catal.* **2013**, *308*, 168.

(42) Bartholomew, C. H.; Farrauto, R. J. *Fundamentals of Industrial Catalytic Processes*, 2nd ed.; John Wiley and Sons: Hoboken, NJ, 2006, p 1.

(43) Chen, M.; Cai, Y.; Yan, Z.; Goodman, D. W. *J. Am. Chem. Soc.* **2006**, *128*, 6341.

(44) Meier, D. C.; Bukhtiyarov, V.; Goodman, A. W. *J. Phys. Chem. B* **2003**, *107*, 12668.

(45) Meier, D. C.; Goodman, D. W. *J. Am. Chem. Soc.* **2004**, *126*, 1892.

(46) Hartshorn, H.; Pursell, C. J.; Chandler, B. D. *J. Phys. Chem. C* **2009**, *113*, 10718.

(47) Pursell, C. J.; Hartshorn, H.; Ward, T.; Chandler, B. D.; Boccuzzi, F. *J. Phys. Chem. C* **2011**, *115*, 23880.

(48) Pursell, C. J.; Chandler, B. D.; Manzoli, M.; Boccuzzi, F. *J. Phys. Chem. C* **2012**, *116*, 11117.

(49) Ruggiero, C.; Hollins, P. *J. Chem. Soc., Faraday Trans.* **1996**, *92*, 4829.

(50) Green, I. X.; Tang, W. J.; Neurock, M.; Yates, J. T. *Acc. Chem. Res.* **2014**, *47*, 805.

(51) Menegazzo, F.; Pinna, F.; Signoretto, M.; Trevisan, V.; Boccuzzi, F.; Chiorino, A.; Manzoli, M. *Appl. Catal., A* **2009**, *356*, 31.

(52) Menegazzo, F.; Manzoli, M.; Chiorino, A.; Boccuzzi, F.; Tabakova, T.; Signoretto, M.; Pinna, F.; Pernicone, N. *J. Catal.* **2006**, *237*, 431.

(53) Hakim, S. H.; Sener, C.; Alba-Rubio, A. C.; Gostanian, T. M.; O'Neill, B. J.; Ribeiro, F. H.; Miller, J. T.; Dumesic, J. A. *J. Catal.* **2015**, *328*, 75.

(54) Shen, J. Y.; Hill, J. M.; Watwe, R. M.; Spiewak, B. E.; Dumesic, J. A. *J. Phys. Chem. B* **1999**, *103*, 3923.

(55) Kottke, M. L.; Tompkins, H. G.; Greenler, R. G. *Surf. Sci.* **1972**, *32*, 231.

(56) Yates, D. J. C. *J. Colloid Interface Sci.* **1969**, *29*, 194.

(57) Mihaylov, M.; Ivanova, E.; Hao, Y.; Hadjiivanov, K.; Gates, B. C.; Knozinger, H. *Chem. Commun.* **2008**, 175.

(58) Vesecky, S. M.; Xu, X. P.; Goodman, D. W. *J. Vac. Sci. Technol., A* **1994**, *12*, 2114.

(59) Wang, L. C.; Khazaneh, M. T.; Widmann, D.; Behm, R. J. *J. Catal.* **2013**, *302*, 20.

(60) Wang, L. C.; Widmann, D.; Behm, R. J. *Catal. Sci. Technol.* **2015**, *5*, 925.

(61) Min, B. K.; Alemozafar, A. R.; Pinnaduwage, D.; Deng, X.; Friend, C. M. *J. Phys. Chem. B* **2006**, *110*, 19833.

(62) Bondzie, V. A.; Parker, S. C.; Campbell, C. T. *Catal. Lett.* **1999**, *63*, 143.

(63) Frenkel, A. I.; Hills, C. W.; Nuzzo, R. G. *J. Phys. Chem. B* **2001**, *105*, 12689.

(64) Lee, E. L.; Wachs, I. E. *J. Phys. Chem. C* **2007**, *111*, 14410.

(65) Lee, E. L.; Wachs, I. E. *J. Phys. Chem. C* **2008**, *112*, 6487.

(66) Williams, W. D.; Bollmann, L.; Miller, J. T.; Delgass, W. N.; Ribeiro, F. H. *Appl. Catal., B* **2012**, *125*, 206.

(67) Centi, G.; Perathoner, S. *Catal. Today* **2009**, *148*, 191.